Key Points:
- We use Landsat time series to reconstruct the spatial structure of tides on the Great Bahama Bank
- Our method predicts tidal phase and amplitude with estimated errors of 15 min and 0.15 m, respectively
- Our method can produce estimates of tidal lag across a shallow bank with or without site-specific calibration data

Supporting Information:
- Supporting Information S1
- Data Set S1
- Data Set S2
- Data Set S3
- Data Set S4
- Data Set S5
- Data Set S6

Correspondence to:
E. C. Geyman,
egeyman@alumni.princeton.edu

Deriving Tidal Structure From Satellite Image Time Series

Emily C. Geyman[1,2] ID **and Adam C. Maloof[1]** ID

[1]Department of Geosciences, Princeton University, Princeton, NJ, USA, [2]Department of Geosciences, UiT The Arctic University of Norway, Tromsø, Norway

Abstract In shallow coastal regions, tides often control the water flux, which in turn directs sediment transport, nutrient delivery, and geochemical gradients. However, tides in shallow areas are spatially heterogeneous, making it challenging to constrain the geographic structure of tidal phase and amplitude without extensive networks of tide gauges. We present a simple remote sensing method for deriving tidal structure from satellite time series. Our method is based on two observations: (1) Tidally driven variations in water depth can be detected as changes in pixel intensity in optical satellite imagery, and (2) repeating passes by an orbiting satellite capture a region at different phases of the tidal cycle. By stacking multiple satellite acquisitions of a shallow bank, we can compute the relative tidal phase and amplitude for each pixel location, thereby resolving a detailed map of tidal propagation and attenuation. While our method requires a set of local water-depth measurements to calibrate the color-to-depth relationship and compute tidal amplitude (in meters), our method can produce spatial estimates of tidal phase and *relative* amplitude without any site-specific calibration data. As an illustration of the method, we use Landsat imagery to derive the spatial structure of tides on the Great Bahama Bank, estimating tidal phase and amplitude with mean absolute errors of 15 min and 0.15 m, respectively.

1. Introduction

The behavior of oceanic tides on shallow continental shelves—and the implications for topics as broad as the evolution of the Earth-Moon orbit (Coughenour et al., 2009; Hansen, 1982) and the global mixing of the ocean (Munk & Wunsch, 1998)—has occupied the minds of scientists for over a century (Jeffreys & Shaw, 1920; Taylor & Shaw, 1919). The advent of satellite altimetry in the early 1990s revolutionized our understanding of global oceanic tides (Cartwright & Ray, 1990; Egbert & Ray, 2000; Tierney et al., 2000). However, the coarse track spacing (∼100 km) of satellite altimeters means that we depend on models—which assimilate satellite altimetry and tide gauge observations—to obtain continuous tidal predictions. While global tide models can constrain tides within 2 cm in the open ocean (Shum et al., 1997), bathymetric uncertainty and coarse grid spacing cause these models to break down in shallow regions such as the Great Bahama Bank (GBB), where tidal lags can exceed 4 hr over distances as small as 20 km (Figure 1).

Understanding tidal dynamics on shallow shelves is essential for constraining banktop hydrodynamics. Wind- and tide-driven currents on shallow banks control the geographic patterns of erosion and deposition (Purkis et al., 2016), water and sediment chemistry (Swart et al., 2009), sedimentary *facies* (e.g., grain size distributions) (Harris et al., 2015; Purkis et al., 2019; Reijmer et al., 2009), coral health (Nakamura & van Woesik, 2001; Schutter et al., 2010), and even species abundance (Rypel et al., 2007).

Three-dimensional numerical circulation models (e.g., Fringer et al., 2006; Hervouet, 2000; Luo et al., 2013), which now are applied routinely to embayments (Weisberg & Zheng, 2006), banktops (Purkis et al., 2017, 2019), and estuaries (Zheng & Weisberg, 2004), are a powerful tool for understanding water circulation in shallow areas. However, these models typically require bathymetric, wind, and tide data for model initialization and forcing. Available remote sensing and weather reanalysis products may be used to constrain some aspects of these hydrodynamic models. For example, satellite scatterometer data constrain surface winds, and water depth can be derived from satellite imagery in shallow waters with low turbidity (e.g., Geyman & Maloof, 2019; Lyzenga, 1978, 1981; Stumpf et al., 2003). Unfortunately, the geographic structure of tidal phase and amplitude often is unknown *a priori*, and the paucity of tide gauge data often forces the use of low-resolution global tide models in hydrodynamic simulations (e.g., Purkis et al., 2017, 2019).

We present a simple method for extracting tidal structure from satellite time series. Our method is based on two observations. First, tidally driven variations in water depth can be detected as changes in pixel intensity
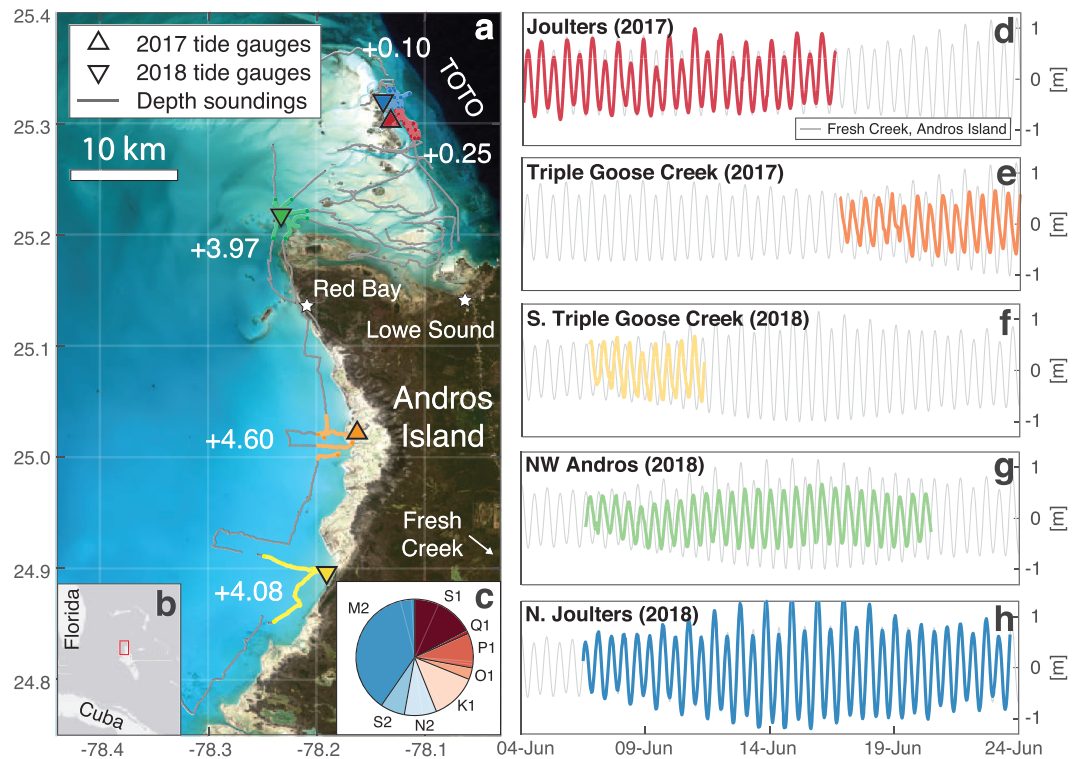
Figure 1. On the Great Bahama Bank (GBB), where sluggish mixing leads to banktop residence times of ~250 days (Broecker & Takahashi, 1966), tidal lags can exceed 4 hr over distances of ≤20 km. (a) A map of the region NW of Andros Island with the tidal lags (in hours) at five tide gauges reported relative to the NOAA tide predictions station at Fresh Creek, Andros Island. "TOTO" stands for "Tongue of the Ocean," the ~1- to 2-km-deep trough east of Andros Island. The gray lines represent the positions of ~300,000 echosounder depth measurements (Geyman & Maloof, 2019a). Only the ~50,000 depth measurements acquired within ≤5 km of a tide gauge, where our understanding of the tides is well constrained, are used as calibration data. (c) The relative contributions of the eight strongest tidal constituents at Fresh Creek. The lunar semidiurnal (M2) tide, with a period of 12.42 hr, is the largest constituent. (d–h) Tide records collected during June 2017 (d and e) and June 2018 (f–h) at the locations shown in (a). The contemporaneous tides at Fresh Creek are shown in gray.

in optical satellite imagery. Second, repeating passes by an orbiting satellite capture a region at different phases of the tidal cycle. Thus, by stacking multiple satellite acquisitions of a shallow bank, we can compute the relative tidal phase and amplitude for each pixel location, thereby resolving a detailed map of tidal propagation and attenuation.

As an illustration of the method, we use Landsat imagery to derive the geographic structure of tides on a portion of the GBB. We choose the GBB as a proof-of-concept study because shallow water carbonate platforms represent the most important ancient archive of sea level, environmental, and ocean geochemical information, so studying modern analog settings such as the Bahamas is a key component of any translation of the rock record into paleoenvironmental interpretations (e.g., Broecker & Takahashi, 1966; Dyer et al., 2018; Geyman & Maloof, 2019b; Harris et al., 2015; Maloof & Grotzinger, 2012; Oehlert et al., 2012; Patterson & Walter, 1994; Swart et al., 2009). It has become clear in modern settings that tidal pumping of water and nutrients plays a critical role controlling the transport and chemistry of carbonate sediment, but global tide models still cannot resolve tidal dynamics on shallow platforms (Shum et al., 1997).

2. Data and Methods

2.1. Study Area and Field Observations

The shallow waters NW of Andros Island on the GBB are well suited for study of spatial variability in tidal structure, since tidal amplitude can vary by a factor of 2 and tidal phase can shift by ~4 hr over distances of ≤20 km (Figure 1). Banktop tides are predominantly semidiurnal, with strong spring-neap amplitude fluctuations (Figures 1c and 4a).
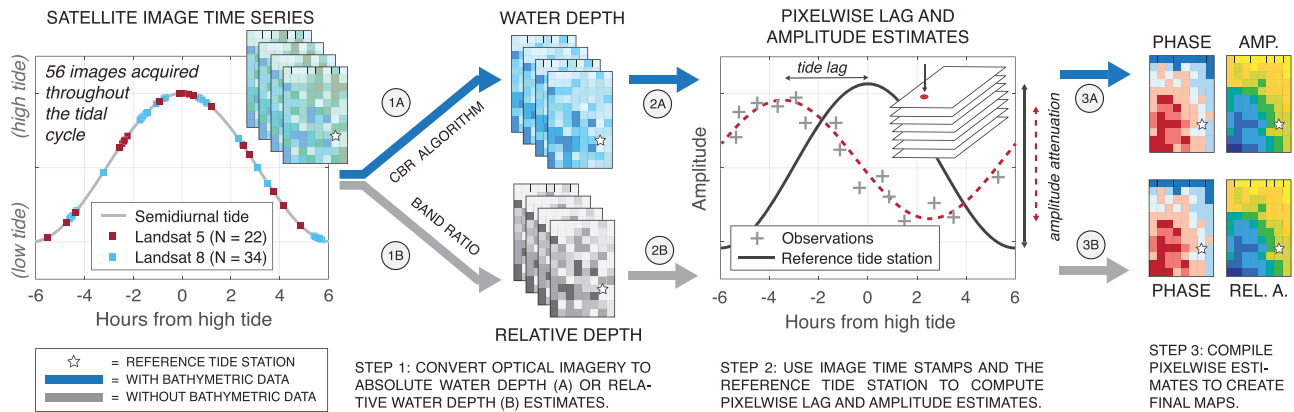
Figure 2. Workflow for estimating tidal structure from satellite time series. (A) depicts the workflow if the user has local bathymetric data. (1A) Use a bathymetric model (e.g., Geyman & Maloof, 2019a), calibrated by local water depth measurements, to compute an instantaneous water depth map from each satellite image. (2A) Use each satellite image's time stamp to compute the hours from high tide at the reference tide station. Estimate the phase lag by fitting a sine wave (with a period equal to the mean tidal period at the reference tide station) to the vector of intensity values for each pixel location. (3A) The phase offset and amplitude of the best-fit sine wave for each pixel provide estimates of local tidal lag and amplitude, respectively. (1B–3B) depict the workflow for computing phase and *relative* amplitude if the user does not have local water depth data. (1B) Convert each multispectral satellite image to a single-channel image in which the pixel intensity is proportional to water depth. See the supporting information, section S5, for a detailed description of this procedure. (2B–3B) Same as (2A–3A), except the amplitude of the sine wave is no longer expressed in units of meters, so the final amplitude map only represents *relative* tidal amplitude.

We use a network of five tide gauges, each recording 5 to 18 days of data in June 2017 and June 2018 (Figures 1d–1h), as ground-truth to evaluate the results of our model. However, only one reference tide gauge is required to implement our method. We use the NOAA tide predictions station at Fresh Creek, Andros Island (Figure 1) as our reference. Note that it is not necessary for the reference tide gauge to be located within the extent of the imagery. The singular requirement is that the tidal character (i.e., the relative mixture of tidal constituents; Figure 1c) at the reference tide gauge is similar to that in the region of interest.

To calibrate the conversion from satellite image color to water depth (see section 2.3), we use ~50,000 depth measurements collected with a BioSonics MX Aquatic Habitat Echosounder (single frequency, 204.8 kHz) (Geyman & Maloof, 2019a).

2.2. Inferring Tidal Structure From Satellite Time Series

Landsat images of the GBB always are acquired at approximately the same time—between 15:20 and 15:40 GMT. However, because tides on the GBB are dominated by the lunar semidiurnal (M2) tide (Figure 1c), the high tide is pushed backward by about 50 min each day. Thus, over time, Landsat images capture the shallow bank at all phases of the tidal cycle (Figure 2).

2.3. Estimating Water Depth From Multispectral Satellite Imagery

Light is attenuated exponentially as it travels through the water column, causing deep water to appear darker than shallow water. Therefore, the color variation in a stack of satellite images records the propagation of tides across a shallow bank. To compute changes in tidal amplitude (in meters) across the banktop, we must convert pixel intensity to water depth. Lyzenga (1978, 1981) proposed a basic algorithm for calculating water depth from satellite imagery, and applications and adaptations of the original Lyzenga algorithm have proven widely successful in shallow waters around the world (Bierwirth & Burne, 1993; Dierssen et al., 2003; Kerr & Purkis, 2018; Lyzenga et al., 2006; Mumby et al., 1998; Philpot, 1989; Polcyn et al., 1970; Stumpf et al., 2003).

We use a simple modification of the Lyzenga (1978) linear algorithm in which we segment the satellite image into zones of spectral homogeneity and calibrate different color-to-depth relationships for each zone before applying a fuzzy *k*-nearest neighbor fit to solve for the final bathymetry. This *cluster-based regression* (CBR) method of Geyman and Maloof (2019a) reduces error by ≥40% relative to previous bathymetric estimates for the region in Figure 1 (Geyman & Maloof, 2019a), since it better accounts for variability in the spectral properties of the sea floor. When applied to the 56 Landsat images in our compilation, the CBR method produces depth estimates with mean absolute errors (MAEs) of 0.14–0.26 m and R^2 values of 0.70–0.88 (Figure 3; Table S1).
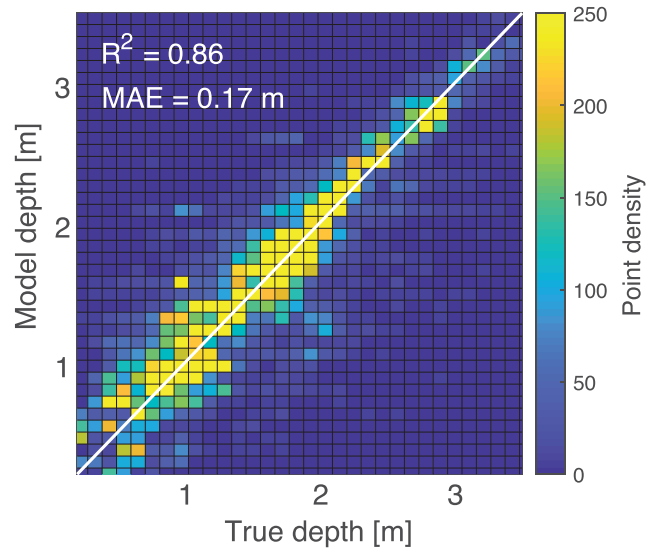
Figure 3. Example model results for the *cluster-based regression* (CBR) bathymetry algorithm (Geyman & Maloof, 2019a) applied to a Landsat 8 image acquired on 20 March 2018. The "true depth" (*x* axis) represents tide-corrected echosounder depth measurements acquired within ≤5 km of a tide gauge (Figure 1), and the "model depth" (*y* axis) represents the water depth calculated from the closest pixel in the Landsat image (30-m resolution). The mean absolute error (MAE) and R^2 values are evaluated on a random 20% subset of the ground-truth data withheld from model training.

2.4. Correcting for Spring-Neap Amplitude Fluctuations

The 56 Landsat images in our compilation sample all portions of the tidal cycle (Figure 2). Of course, each Landsat acquisition captures a *different* tidal cycle, since the revisit period of Landsat satellites is 16 days. Tidal amplitude on the GBB varies by nearly a factor of 2 over the course of a typical bimonthly spring-neap cycle (Figure 4a). Therefore, to facilitate comparison between images captured from neap to spring tide, we scale all Landsat-derived estimates of tidal amplitude by $\bar{A}_{FC}/A_{FC}$, where $\bar{A}_{FC}$ is the *mean* tidal amplitude at Fresh Creek (0.93 m) and A_{FC} is the *contemporaneous* tidal amplitude at Fresh Creek. For example, if a particular Landsat-derived tidal estimate is +0.3 m for a given location on the bank, but the tide station at Fresh Creek indicates that the tidal amplitude on the day of image acquisition was just 0.50 m, the tidal offset observation at the pixel of interest will be scaled by 0.93/0.50.
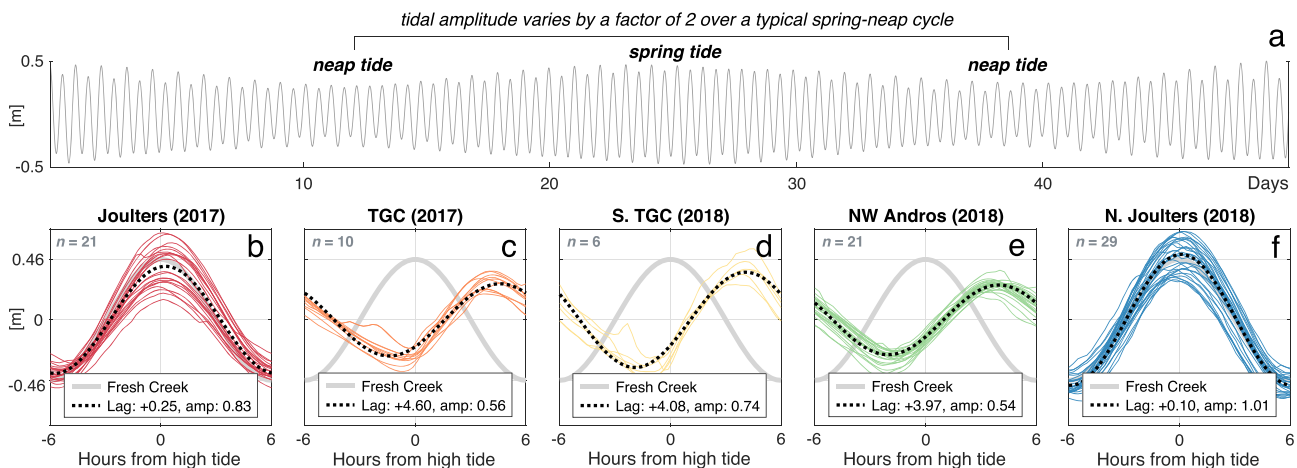

Figure 4. (a) An example 50-day tide record from Fresh Creek. Note that tidal amplitude varies by a factor of 2 over a typical spring-neap cycle. (b–f) A superposition of all the semidiurnal tide cycles observed at our five tide gauge stations in Figure 1. *n* represents the length (in days) of each record. The *x* axis denotes hours from high tide at Fresh Creek. The mean lag is reported in hours relative to Fresh Creek, and the mean amplitude (scaled to the contemporaneous Fresh Creek record to account for spring-neap variations in tidal amplitude—see section 2.4) is reported in meters. For reference, the mean tidal amplitude at Fresh Creek is 0.93 m.
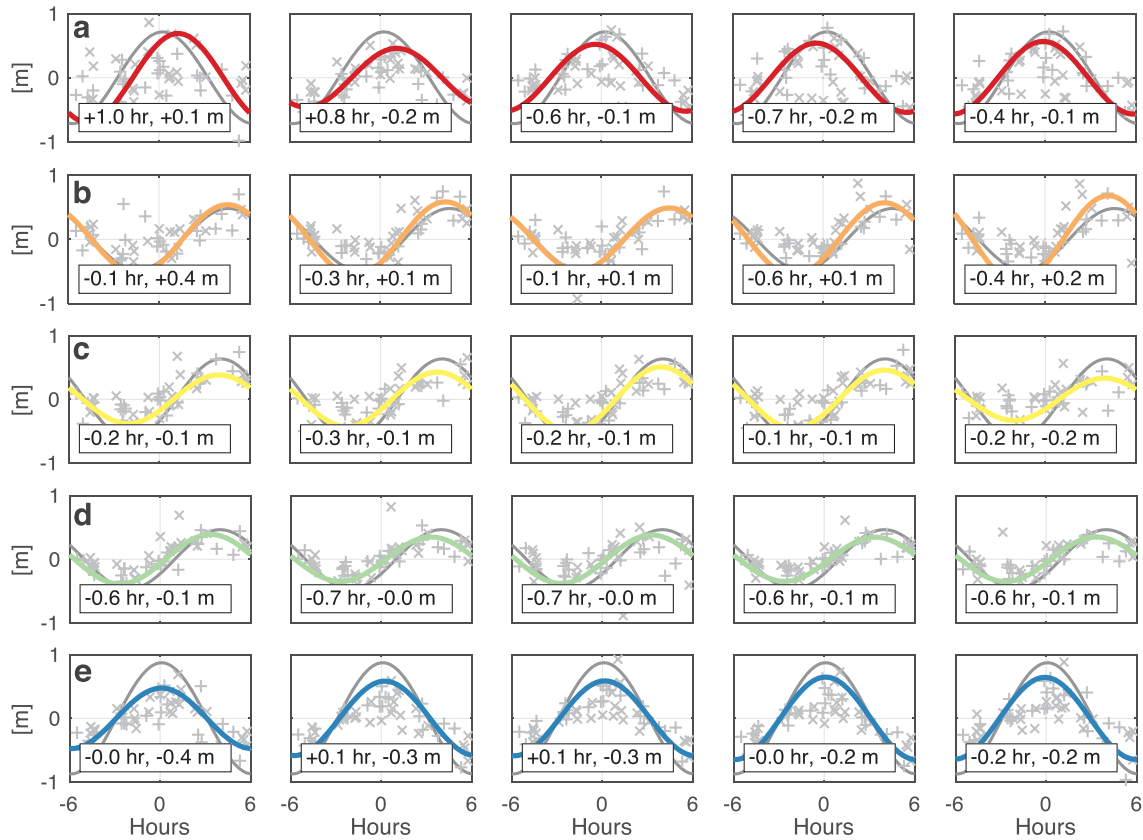
Figure 5. A comparison between the true tidal phase and amplitude at each tide gauge (gray lines) and model estimates (colored lines) for 5 random pixels adjacent to each tide gauge. Each column represents a different pixel location. Each row represents a different tide gauge: (a) Joulters 2017, (b) TGC 2017, (c) S. TGC 2018, (d) NW Andros 2018, and (e) N. Joulters 2018 (Figure 1). The final error estimates (Table 1) reflect the comparison between tide gauge records and ~200 random pixel locations within 500 m of each tide gauge. To prevent biasing our error estimates, we exclude bathymetric data acquired near a given tide gauge when estimating error for that particular tide gauge. For example, in (a), which represents model predictions for the Joulters (2017) tide record, only bathymetric data acquired near the other four tide gauges were used to calibrate the CBR algorithm (section 2.3). The gray "+" marks, and "x" marks indicate depth estimates from Landsat 5 and Landsat 8 acquisitions, respectively. The text box shows the phase and amplitude error for each sinusoidal fit (colored line).

2.5. Computing Tidal Phase and Amplitude

In regional and global tide models, tides typically are defined in terms of the amplitudes (meters) and phases (radians or degrees) of a set of tidal constituents, such as the lunar semidiurnal (M2) and solar diurnal (S1) tides (Lyard et al., 2006). Our 56 sets of Landsat-derived water depth estimates are too sparse (and temporally incoherent) to compute the phase and amplitude parameters of the prominent tidal constituents for each pixel. Therefore, we describe GBB tides in terms of a phase lag and amplitude change from the tides at Fresh Creek (Figure 4).

Table 1
Errors of the Model-Predicted Phase and Amplitude for Each of the Five Tide Gauge Locations in Figure 1

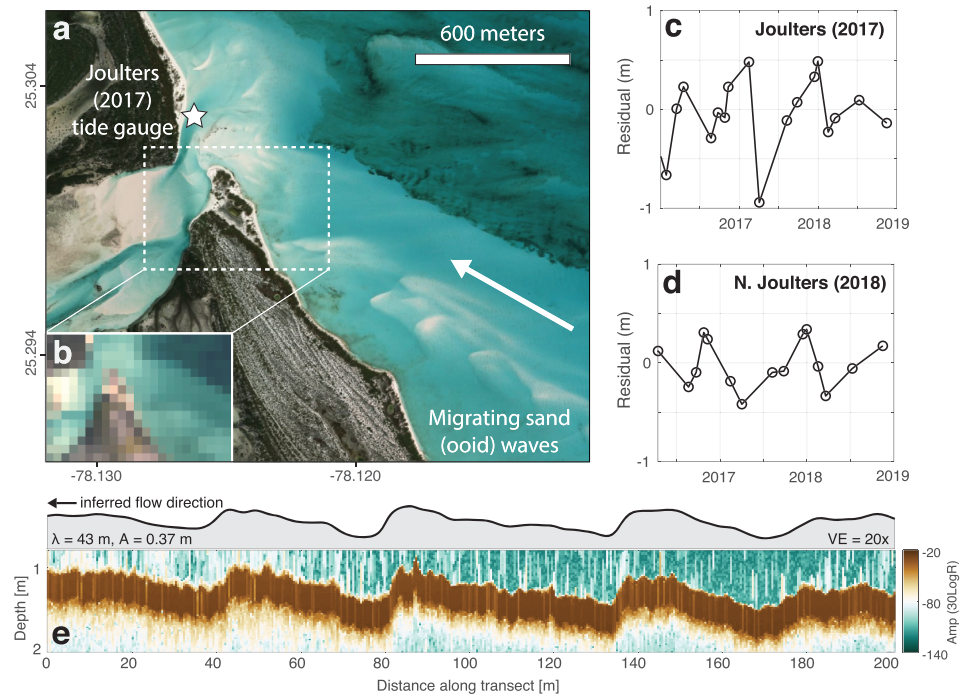|	With depth data		Without depth data
Location	Error (hr)	Error (m)	Error (hr)
Joulters (2017)	+0.08	−0.15	−0.49
TGC (2017)	−0.48	+0.06	+0.77
S. TGC (2018)	−0.03	−0.12	−1.44
NW Andros (2018)	−0.43	−0.08	−0.49
N. Joulters (2018)	+0.19	−0.32	+0.69
Mean absolute error	0.25	0.15	0.78

Figure 6. The Joulters tide gauge sites (Figure 1) are located in a highly-active region of the Great Bahama Bank, where migrating oolitic sand waves cause systematic changes in water depth over time. (a) A mosaic of high-resolution satellite imagery, courtesy of ESRI, shows sand waves in the central Joulters Cay region. (b) The 30-m Landsat images are too coarse to resolve the boundaries of individual bedforms. However, subtle changes in pixel intensity (and inferred water depth) may record migration of the sand waves. (c-d) The residual between the point observations and sinusoidal fits in Figure 5a (Joulters 2017) and Figure 5e (N. Joulters 2018) show patterns consistent with migrating sand bodies. Specifically, the annual $\sim$ 0.5-1.0 m variations in water depth in (c) and (d) suggest the passing of one 0.5-1.0 m bedform roughly each year. (e) A 200-m echosounder transect in the N. Joulters region (Figure 1) captures long-wavelength, low-amplitude ($\lambda \approx 43$, A $\approx$ 0.37 m) subaqueous dunes that are similar to the migrating bedforms recorded in (c-d).

Figure 2 summarizes our method of inferring tidal phase and amplitude either (A) with or (B) without local water depth data. If local water depth data are available, we use the CBR algorithm to generate a bathymetric map for each of the 56 Landsat images (section 2.3). Thus, for every pixel location on the bank, we obtain a vector of 56 water depth estimates (and their associated uncertainties) and a corresponding vector of positions in the tidal cycle (measured as hours from high tide at Fresh Creek). We use the Nelder-Mead multidimensional unconstrained nonlinear minimization algorithm (Nelder & Mead, 1965) to solve for the best fit sine wave with a 12.42-hr period. Note that 12.42 hours is not only the period of the dominant tidal constituent at Fresh Creek (M2, Figure 1c) but also the mean tidal period observed in 13 years of high/low tide data for Fresh Creek (Figure S6). For each pixel location, the sine wave's phase offset from the Fresh Creek reference provides an estimate of tidal lag, and the sine wave's amplitude records the local tidal amplitude. If local bathymetric data are not available, we cannot use the CBR algorithm to map spectral reflectance to water depth. However, our method still can be used to generate estimates of tidal phase and *relative* amplitude (Figure 2).

3. Results
3.1. Model Validation
To evaluate the accuracy of our tide model, we compare the predictions of tidal phase and amplitude to the measured values at each of our five gauges (Figure 1). Note that we use the tide gauge records to correct bathymetric data used in the CBR algorithm (section 2.3). Therefore, to ensure a fully independent evaluation of model accuracy, we iteratively train the tide model using bathymetric data adjacent to four of the five tide gauges. We then compare the estimated phase and amplitude at the location of the held-out tide gauge to the ground-truth measurements. Figure 5 compares the model-derived tide estimates at five nearby pixel locations to the true tidal phase and amplitude. The tide model that incorporates local bathymetric data
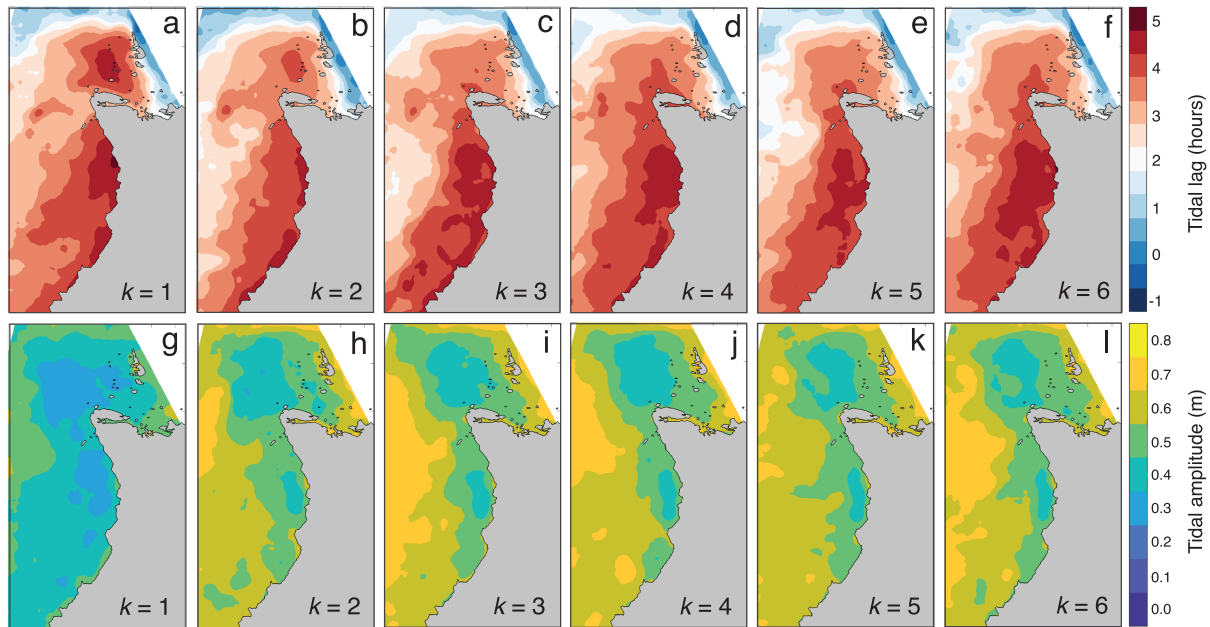
Figure 7. Sensitivity of the estimated tidal phase and amplitude to k, the number of spectral clusters used in the CBR algorithm (Geyman & Maloof, 2019a). For $k \geq 2$, all values of k yield similar predictions for tidal phase (a-f) and amplitude (g-l).

yields MAEs for tidal phase and amplitude of 0.25 hr and 0.15 m, respectively. The tide model that does not rely on any local ground-truth data produces a larger average error of 0.78 hr (Table 1).

The typical scatter of ≤0.3 m about the sinusoidal fits in Figure 5 is unsurprising given that the bathymetric model, which maps image color to water depth (Figure 3), has a MAE of 0.14–0.26 m (Table S1). However, some of the noise in the records of tidal position versus water depth may be caused by real changes in bathymetry during the 14-year Landsat time series. The high-energy Joulter Cays region, which experiences water depth changes on diurnal to annual timescales caused by migrating subaqueous dunes and ooid shoals (Figure 6), produces noisier records than the other sites (Figure 5). The 30-m resolution of the Landsat images is too coarse to resolve small sand bodies (Figure 6b), but time series analysis of the residuals between the individual depth observations and the sinusoidal fits in Figure 5 shows patterns consistent with migrating ooid shoals (Figures 6c–6e). Thus, the *residuals* in tidal amplitude may provide a window into understanding the timescales of bedform migration and sediment flux. Moreover, while the elevated noise in the Joulters sites causes the tidal amplitude to be underestimated, the tidal lags at those sites are still correct to within ≤0.19 hr (11 min) (Table 1).

3.2. Model Sensitivity

The only tunable parameter in our tide model is k, the number of spectral clusters used during the conversion of reflectance to water depth in the CBR algorithm. Beyond $k = 1$, all models converge on similar tidal phase and amplitude estimates (Figure 7). Therefore, because Geyman and Maloof (2019a) showed that models with lower k values perform better when extrapolating from limited calibration data sets, we use $k = 2$.

3.3. Spatial Structure of Tidal Phase and Amplitude

Figures 8a and 8b show the tide model's phase and amplitude predictions for the GBB. The lag relative to Fresh Creek is close to zero along the margin closest to the Tongue of the Ocean (Figure 1). The shallow waters on the west side of Andros Island and Joulter Cays permit long lags (~4 hr) and small tidal amplitudes (~0.3 m). If no local bathymetric data were available, we could generate similar predictions of tidal lag and *relative* amplitude (Figures 8c and 8d). The two predictions of tidal lag typically differ by ≤1 hr (Figure S4).

3.4. Uncertainty Analysis

To understand the uncertainty associated with the tide estimates in Figure 8, we apply a bootstrap resampling approach in which, for each pixel, we fit a sine wave to a random sample of 70% the data (40 of the 56 Landsat-derived depth estimates). We repeat this procedure with 20 random subsamples and then report the interquartile range (25th to 75th percentile) in tidal lag and amplitude. Figure 9 illustrates that shallow
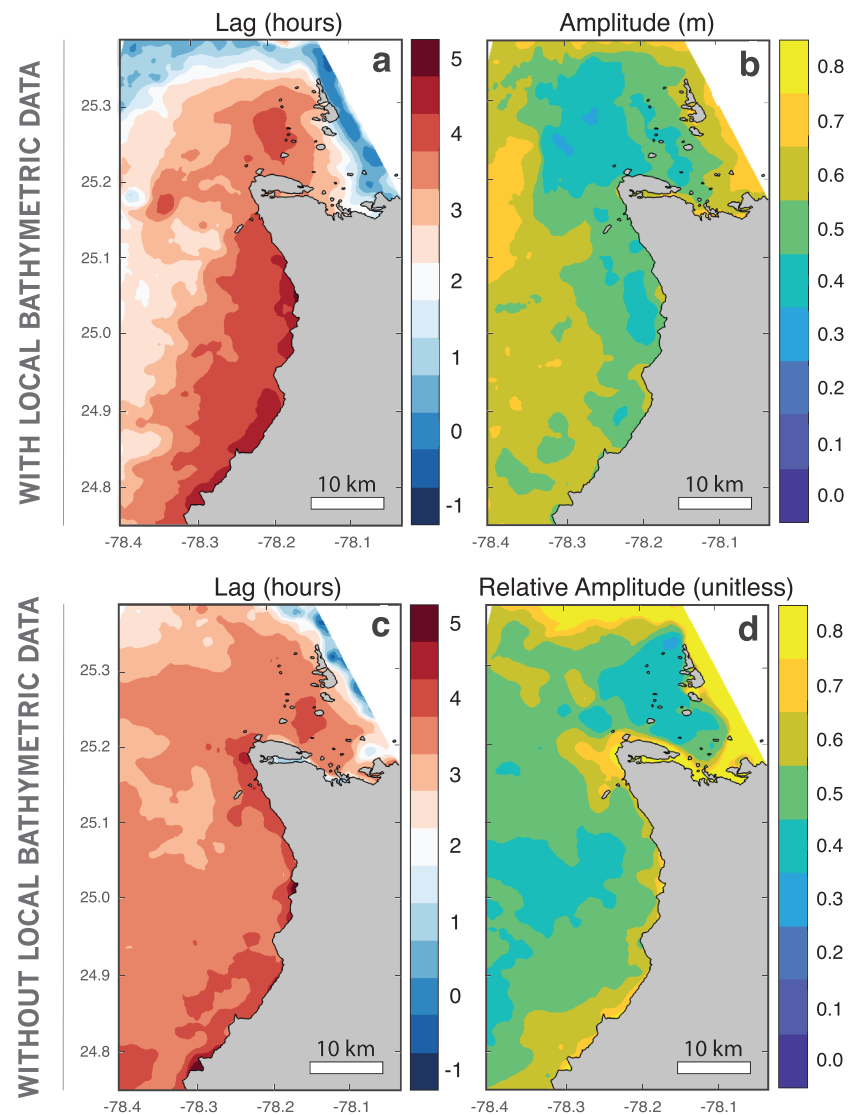
Figure 8. Spatial structure of tidal phase (a) and amplitude (b) generated by the tide model that uses local water depth data (Figure 2A). Notice that the majority of the phase lag and amplitude attenuation occurs within ~10 km of the shelf break where the GBB gives way to the Tongue of the Ocean (Figure 1). If no local bathymetric data were available, we could generate similar predictions of lag (c) and *relative* amplitude (d). The phase estimates in (a) and (c) typically differ by ≤1 hr (Supplementary Information, Figure S4).

waters support the smallest uncertainties in both tidal lag and amplitude, which likely is because the CBR algorithm performs best in shallow waters (Geyman & Maloof, 2019a).

4. Discussion

Regions such as the GBB, with very shallow waters and significant restriction from the global ocean, have eluded previous attempts at modeling tides from remote sensing data. On the GBB, the gradients in tidal phase are too steep to resolve directly from satellite altimetry missions, which often have track spacing ≥100 km (~315-, ~140-, and ~80-km spacing at the equator for TOPEX/Poseidon, JASON-1, and ERS5 1, respectively). Tide models assimilating satellite altimetry data with the barotropic shallow-water equations provide tidal estimates with complete banktop coverage. However, coarse grid spacing and large relative bathymetric errors cause these models to be inaccurate in shallow waters (Shum et al., 1997). For example, the high-resolution (0.125° × 0.125°) global tide model FES2014 (Carrere et al., 2015) predicts 0 min of tide lag and no amplitude attenuation between Joulter Cays and Triple Goose Creek (TGC), where we document 4.5 hours of lag and 45% reduction in tidal amplitude (Figure 4).
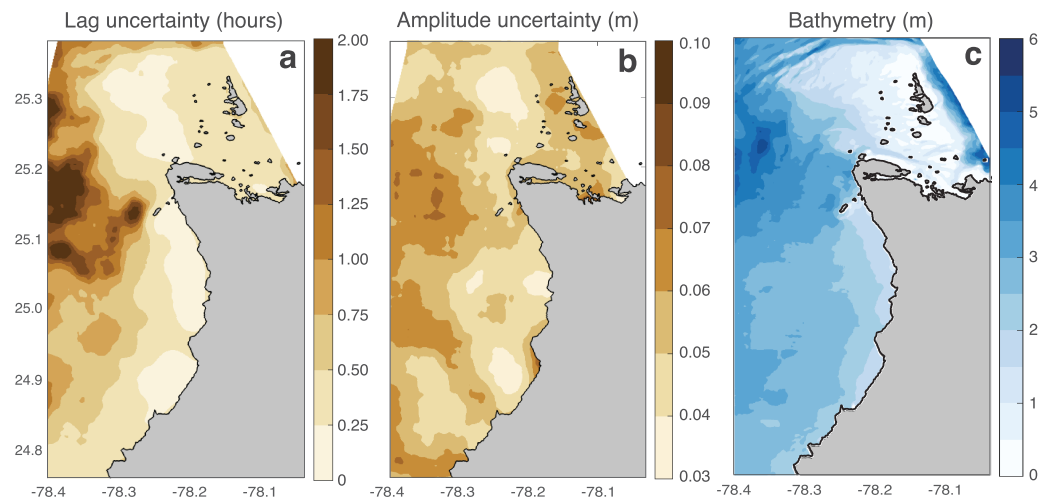
Figure 9. Uncertainty estimates for the tidal lag and amplitude predictions in Figures 8a and 8b. We quantify uncertainty as the interquartile range of lag (a) and amplitude (b) estimates obtained by iteratively applying the tide model to random subsets of the Landsat data set (section 3.3). Both tidal lag and amplitude are poorly constrained for the deeper waters along the western margin of the study area, which may reflect the fact that the conversion from pixel intensity to water depth is less accurate in deeper waters (Figure S5). (c) Bathymetry from Geyman and Maloof (2019a).

The fact that global tide models, which now boast errors of <2 cm for the open ocean (Shum et al., 1997), remain inaccurate for shallow waters is important for two reasons. First, accurate representation of bank-top tides is necessary for forcing hydrodynamic models, which enable understanding of the link between water flux, geochemical gradients, sediment transport, and biosedimentary facies. Even our tidal estimates that require no site-specific calibration data (Figures 8c and 8d) are capable of representing the banktop tidal propagation and attenuation missed by global models such as FES2014. Second, shallow shelves are significant contributors to the global budget of tidal dissipation (Egbert et al., 2004). Our simple method for estimating tidal structure could be scaled up and applied to coarser optical imagery such as MODIS in order to quantify tidal dissipation in shallow water regions across the globe.

Although freely available Landsat images yield empirical tidal estimates with continuous coverage and 30-m resolution, our optical method suffers from a number of disadvantages compared to the altimetric method. First, optically derived tidal estimates are sensitive to changes in water turbidity, which may vary with tidal phase, potentially biasing the retrieved tidal signal and restricting application to clear (nonturbid) waters like those of the GBB. Second, optical tidal estimates are susceptible to changes in local bathymetry and bottom reflectance. Real changes in benthic character over the 14-year Landsat time series (Figure 2) may violate the assumption that changes in each pixel's reflectance represent tidally driven changes in water depth (Figure 5) and may contribute to the uncertainty of our final estimates. However, new laser altimetry data from ICESat-2 (Abdalati et al., 2010), which can provide elevation estimates for both the sea surface and sea bottom (Forfinski-Sarkozi & Parrish, 2016), could serve as a cross-calibration for optically derived tidal estimates. Moreover, the optical method's sensitivity to seabed properties also represents one of its greatest strengths, since our approach can be used to quantify sediment transport (Figure 6) and changes to benthic ecology on decadal time scales.

References

Abdalati, W., Zwally, H. J., Bindschadler, R., Csatho, B., Farrell, S. L., Fricker, H. A., et al. (2010). The ICESat-2 laser altimetry mission. *Proceedings of the IEEE*, *98*(5), 735–751.

Bierwirth, P., & Burne, R. V. (1993). Shallow sea-floor reflectance and water depth derived by unmixing multispectral imagery. *Photogrammetric Engineering & Remote Sensing*, *59*(3), 331–338.

Broecker, W., & Takahashi, T. (1966). Calcium carbonate precipitation on the Bahama Banks. *Journal of Geophysical Research*, *71*(6), 1575–1602.

Carrere, L., Lyard, F., Cancet, M., & Guillot, A. (2015). FES 2014, a new tidal model on the global ocean with enhanced accuracy in shallow seas and in the Arctic region. In *EGU General Assembly Conference Abstracts*, EGU General Assembly Conference Abstracts, *17*, pp. 5481.

Cartwright, D. E., & Ray, R. D. (1990). Oceanic tides from Geosat altimetry. *Journal of Geophysical Research*, *95*(C3), 3069–3090.

Coughenour, C. L., Archer, A. W., & Lacovara, K. J. (2009). Tides, tidalites, and secular changes in the Earth Moon system. *Earth-Science Reviews*, *97*(1), 59–79.

Dierssen, H. M., Zimmerman, R. C., Leathers, R. A., Downes, T. V., & Davis, C. O. (2003). Ocean color remote sensing of seagrass and bathymetry in the Bahamas Banks by high-resolution airborne imagery. *Limnology and Oceanography*, *48*(1part2), 444–455.

Dyer, B., Maloof, A. C., Purkis, S. J., & Harris, P. M. (2018). Quantifying the relationship between water depth and carbonate facies. *Sedimentary Geology*, *373*, 1–10.

Egbert, G. D., & Ray, R. D. (2000). Significant dissipation of tidal energy in the deep ocean inferred from satellite altimeter data. *Nature*, *405*, 775–778.

Egbert, G. D., Ray, R. D., & Bills, B. G. (2004). Numerical modeling of the global semidiurnal tide in the present day and in the last glacial maximum. *Journal of Geophysical Research*, *109*, C03003. https://doi.org/10.1029/2003JC001973

Forfinski-Sarkozi, N. A., & Parrish, C. E. (2016). Analysis of MABEL bathymetry in Keweenaw Bay and implications for ICESat-2 ATLAS. *Remote Sensing*, *8*(9), 772.

Fringer, O. B., Gerritsen, M., & Street, R. L. (2006). An unstructured-grid, finite-volume, nonhydrostatic, parallel coastal ocean simulator. *Ocean Modelling*, *14*(3), 139–173.

Geyman, E. C., & Maloof, A. C. (2019a). A simple method for extracting water depth from multispectral satellite imagery in regions of variable bottom type. *Earth and Space Science*, *6*, 527–537.

Geyman, E. C., & Maloof, A. C. (2019b). A diurnal carbon engine explains ^{13}C-enriched carbonates without increasing the global production of oxygen. *Proceedings of the National Academy of Sciences*, *116*(49), 24,433–24,439.

Hansen, K. S. (1982). Secular effects of oceanic tidal dissipation on the Moon's orbit and the Earth's rotation. *Reviews of Geophysics*, *20*(3), 457–480.

Harris, P. M., Purkis, S. J., Ellis, J., Swart, P. K., & Reijmer, J. J. G. (2015). Mapping bathymetry and depositional facies on Great Bahama Bank. *Sedimentology*, *62*(2), 566–589.

Hervouet, J.-M. (2000). TELEMAC modelling system: An overview. *Hydrological Processes*, *14*(13), 2209–2210.

Jeffreys, H., & Shaw, W. N. (1920). VIII. Tidal friction in shallow seas. *Philosophical Transactions of the Royal Society of London. Series A, Containing Papers of a Mathematical or Physical Character*, *221*(582-593), 239–264.

Kerr, J. M., & Purkis, S. (2018). An algorithm for optically-deriving water depth from multispectral imagery in coral reef landscapes in the absence of ground-truth data. *Remote Sensing of Environment*, *210*, 307–324.

Luo, J., Li, M., Sun, Z., & O'Connor, B. A. (2013). Numerical modeling of hydrodynamics and sand transport in the tide-dominated coastal-to-estuarine region. *Marine Geology*, *342*, 14–27.

Lyard, F., Lefevre, F., Letellier, T., & Francis, O. (2006). Modelling the global ocean tides: Modern insights from FES2004. *Ocean Dynamics*, *56*(5), 394–415.

Lyzenga, D. R. (1978). Passive remote sensing techniques for mapping water depth and bottom features. *Applied Optics*, *17*(3), 379–383.

Lyzenga, D. R. (1981). Remote sensing of bottom reflectance and water attenuation parameters in shallow water using aircraft and Landsat data. *International Journal of Remote Sensing*, *2*(1), 71–82.

Lyzenga, D. R., Malinas, N. P., & Tanis, F. J. (2006). Multispectral bathymetry using a simple physically based algorithm. *IEEE Transactions on Geoscience and Remote Sensing*, *44*(8), 2251–2259.

Maloof, A. C., & Grotzinger, J. P. (2012). The Holocene shallowing-upward parasequence of north-west Andros Island, Bahamas. *Sedimentology*, *59*, 1375–1407.

Mumby, P. J., Clark, C. D., Green, E. P., & Edwards, A. J. (1998). Benefits of water column correction and contextual editing for mapping coral reefs. *International Journal of Remote Sensing*, *19*(1), 203–210.

Munk, W., & Wunsch, C. (1998). Abyssal recipes II: Energetics of tidal and wind mixing. *Deep Sea Research Part I: Oceanographic Research Papers*, *45*(12), 1977–2010.

Nakamura, T., & van Woesik, R. (2001). Water-flow rates and passive diffusion partially explain differential survival of corals during the 1998 bleaching event. *Marine Ecology Progress Series*, *212*, 301–304.

Nelder, J. A., & Mead, R. (1965). A simplex method for function minimization. *The Computer Journal*, *7*(4), 308–313.

Oehlert, A. M., Lamb-Wozniak, K. A., Devlin, Q. B., Mackenzie, G. J., Reijmer, JohnJ. G., & Swart, P. K. (2012). The stable carbon isotopic composition of organic material in platform derived sediments: Implications for reconstructing the global carbon cycle. *Sedimentology*, *59*(1), 319–335.

Patterson, W. P., & Walter, L. M. (1994). Depletion of 13C in seawater DIC on modern carbonate platforms: significance for the carbon isotopic record of carbonates. *Geology*, *22*(2), 885–888.

Philpot, W. D. (1989). Bathymetric mapping with passive multispectral imagery. *Applied Optics*, *28*(8), 1569–1578.

Polcyn, F. C., Brown, W. L., & Sattinger, I. J. (1970). The measurement of water depth by remote-sensing techniques (*8973-26-F*): Willow Run Laboratories, University of Michigan.

Purkis, S., Cavalcante, G., Rohtla, L., Oehlert, A. M., Harris, P. M., & Swart, P. K. (2017). Hydrodynamic control of whitings on Great Bahama Bank. *Geology*, *45*(10), 939.

Purkis, S., Harris, P. M., & Cavalcante, G. (2019). Controls of depositional facies patterns on a modern carbonate platform: Insight from hydrodynamic modeling. *The Depositional Record*, *5*, 421–437.

Purkis, S., Van de Koppel, J., & Burgess, P. M. (2016). Autogenic dynamics and self-organization in sedimentary systems. (p. 53-66) Society for Sedimentary Geology.

Reijmer, J. J. G., Swart, P. K., Bauch, T., Otto, R., Reuning, L., Roth, S., & Zechel, S. (2009). A re-evaluation of facies on Great Bahama Bank I: New facies maps of western Great Bahama Bank. *Perspectives in Carbonate Geology*, *41*, 29–46.

Rypel, A. L., Layman, C. A., & Arrington, D. A. (2007). Water depth modifies relative predation risk for a motile fish taxon in Bahamian tidal creeks. *Estuaries and Coasts*, *30*(3), 518–525.

Schutter, M., Croker, J., Paijmans, A., Janse, M., Osinga, R., Verreth, A. J., & Wijffels, R. H. (2010). The effect of different flow regimes on the growth and metabolic rates of the scleractinian coral Galaxea fascicularis. *Coral Reefs*, *29*, 737–748.

Shum, C. K., Woodworth, P. L., Andersen, O. B., Egbert, G., Francis, O., King, C., et al. (1997). Accuracy assessment of recent ocean tide models. *Journal of Geophysical Research*, *102*, 173–194.

Stumpf, R. P., Holderied, K., & Sinclair, M. (2003). Determination of water depth with high-resolution satellite imagery over variable bottom types. *Limnology and Oceanography*, *48*(1), 547–556.

Swart, P. K., Reijmer, J. J. G., & Otto, R. (2009). A re-evaluation of facies on Great Bahama Bank II: Variations in the δ^{13}C, δ^{18}O and mineralogy of surface sediments. *International Association of Sedimentologists Special Publication*, *41*, 47–59.

Taylor, G. I., & Shaw, W. N. (1919). I. Tidal friction in the Irish Sea. *Philosophical Transactions of the Royal Society of London. Series A, Containing Papers of a Mathematical or Physical Character*, *220*(571-581), 1–33.

Tierney, C. C., Kantha, L. H., & Born, G. H. (2000). Shallow and deep water global ocean tides from altimetry and numerical modeling. *Journal of Geophysical Research*, *105*(11), 259–277.

Weisberg, R. H., & Zheng, L. (2006). Circulation of tampa bay driven by buoyancy, tides, and winds, as simulated using a finite volume coastal ocean model. *Journal of Geophysical Research*, *111*, C01005. https://doi.org/10.1029/2005JC003067

Zheng, L., & Weisberg, R. H. (2004). Tide, buoyancy, and wind-driven circulation of the Charlotte Harbor estuary: A model study. *Journal of Geophysical Research*, *109*, C06011. https://doi.org/10.1029/2003JC001996